NO EVIDENCE FOR CHEMICAL ABUNDANCE VARIATIONS IN THE INTERMEDIATE-AGE CLUSTER NGC 1783

Hao Zhang,[1] Richard de Grijs,[1,2] Chengyuan Li,[3] and Xiaohan Wu[1,4]

[1] *Kavli Institute for Astronomy & Astrophysics and Department of Astronomy, School of Physics, Peking University, Yi He Yuan Lu 5, Hai Dian District, Beijing 100871, China*

[2] *International Space Science Institute–Beijing, 1 Nanertiao, Zhongguancun, Hai Dian District, Beijing 100190, China*

[3] *Department of Physics and Astronomy, Macquarie University, Sydney, NSW 2109, Australia*

[4] *Harvard-Smithsonian Center for Astrophysics, Harvard University, Cambridge, MA 02138, USA*

ABSTRACT

We have analyzed multi-passband photometric observations, obtained with the *Hubble Space Telescope*, of the massive (1.8×10^5 $M_\odot$), intermediate-age (1.8 Gyr-old) Large Magellanic Cloud star cluster NGC 1783. The morphology of the cluster's red giant branch does not exhibit a clear broadening beyond its intrinsic width; the observed width is consistent with that owing to photometric uncertainties alone and independent of our photometric selection boundaries applied to obtain our sample of red-giant stars. The color dispersion of the cluster's red-giant stars around the best-fitting ridgeline is 0.062 ± 0.009 mag, which is equivalent to the width of 0.080 ± 0.001 mag derived from artificial simple stellar population tests, that is, tests based on single-age, single-metallicity stellar populations. NGC 1783 is comparably massive as other star clusters that show clear evidence of multiple stellar populations. After incorporating mass-loss recipes from its current age of 1.8 Gyr to an age of 6 Gyr, NGC 1783 is expected to remain as massive as some other clusters that host clear multiple populations at these intermediate ages. If we were to assume that mass is an important driver of multiple population formation, then NGC 1783 should have exhibited clear evidence of chemical abundance variations. However, our results support the absence of any chemical abundance variations in NGC 1783.

Keywords: stars: abundances – globular clusters: individual: NGC 1783 – Hertzsprung-Russell and color-magnitude diagrams – galaxies: individual: Large Magellanic Cloud

1. INTRODUCTION

Star clusters were long believed to be composed of simple stellar population (SSPs). That is, they were thought to consist of stars that were all formed at approximately the same time in a single starburst event from a common progenitor giant molecular cloud. This would also imply that all of their stars should have similar metallicities (Vesperini et al. 2013; Bastian & Strader 2014; Cabrera-Ziri et al. 2014; Li et al. 2016b; Hong et al. 2017). To avoid stochastic sampling effects, statistical studies of star clusters and their stellar populations are often based on clusters with masses exceeding a few $\times 10^4$–10^5 $M_\odot$, thus precluding the use of open clusters in the Milky Way or the Magellanic Clouds for such purposes.

Today, we know that the SSP approximation holds true for at least some star clusters; after all, no evidence of chemical abundance variations has been found among the stars populating most young massive clusters (e.g., Mucciarelli et al. 2008; Cabrera-Ziri et al. 2016). In addition, it has been suggested that rapid star formation will eject member stars and residual gas from young clusters (Bate et al. 2003; Baumgardt & Kroupa 2007; Farias et al. 2015). This is supported by observations of extremely young embedded clusters (Lima et al. 2014) and young massive clusters (Bastian & Goodwin 2006; Davidge 2012; Bastian et al. 2013; Bastian & Strader 2014; Cabrera-Ziri et al. 2015).

However, an ever larger body of observations of old globular clusters (GCs; with ages > 10 Gyr) increasingly challenges this model. For example, studies based on small samples of bright stars in individual clusters have revealed significant star-to-star chemical dispersions that violate the SSP scenario (Shetrone 1996; Carretta et al. 2004; Gratton et al. 2004; Carretta et al. 2009). Photometric and spectroscopic analyses of massive star clusters have provided additional support for the presence of intra-cluster chemical abundance dispersions (Worthey 1994; Shetrone 1996; Bedin et al. 2000; Piotto et al. 2007; Marino et al. 2008; Anderson et al. 2009; Piotto et al. 2013).

Given that most young massive clusters appear to be clean SSPs, while many old GCs show evidence of containing multiple stellar populations (MSPs), the key questions of interest become at which age the MSP phenomenon first makes an appearance, and whether age is indeed the crucial parameter driving the emergence of MSPs. That is, is there a critical age at which the transition from SSPs to MSPs occurs? Could mass be an alternative parameter? The latter scenario may not be as far-fetched as it might appear at first sight: indeed, if MSPs originate primarily from colliding asymptotic giant-branch (AGB) stellar winds, one would expect MSPs to only form in clusters that are sufficiently massive to retain the AGB ejecta in their gravitational potential wells.

In the context of cluster formation through an initial starburst (e.g., Vesperini et al. 2013; Bastian & Strader 2014; Cabrera-Ziri et al. 2014; Hong et al. 2017), the presence of MSPs would be primarily associated with the formation mechanism of second-generation stars. Most related scenarios suggest that these second-generation stars would be characterized by broad distributions of chemical abundances, because they formed from gas that was polluted by the ejecta from first-generation stars. Possible polluters include rapidly rotating massive stars (Charbonnel et al. 2013), supermassive stars (Denissenkov & Hartwick 2014), massive interacting binary systems (Bastian et al. 2015), young AGB stars (D'Ercole et al. 2008), and evolving low-mass binary systems (Jiang et al. 2014).

Alternative scenarios have been proposed which suggest external accretion, including accretion from the interstellar medium (Bekki & Mackey 2009; Pflamm-Altenburg & Kroupa 2009; Li et al. 2016a), accretion of AGB ejecta (Bekki 2017), and cluster mergers (Hong et al. 2017). Unfortunately, the star cluster population in the Milky Way has an extreme age distribution (Harris 1996; McLaughlin & van der Marel 2005), given that most GCs are older than 10 Gyr, while only a handful of similarly massive clusters are younger than a few $\times 10^8$ yr. Therefore, the massive cluster population in the Milky Way cannot be used to test whether MSPs emerge with increasing cluster age. Similarly, in the Large Magellanic Cloud (LMC), a well-known 'age gap' exists in the cluster age distribution, with a dearth of clusters in the 2–6 Gyr age range (Geisler et al. 1997; Balbinot et al. 2010).

Fortunately, the combined sample of massive clusters in the LMC and the Small Magellanic Cloud (SMC) includes a number of objects in the 2–6 Gyr range (Milone et al. 2009). Specifically, six star clusters from the McLaughlin & van der Marel 2005 catalog fall in this age range, including NGC 2121, Hodge 4, NGC 2155, NGC 2193, SL 663, and Kron 3. The youngest star cluster that has been found to show evidence of MSPs is NGC 1978 (Martocchia et al. 2018). It has an age close to 2 Gyr. Therefore, assuming that age is a key driver of the MSP phenomenon, its onset appears to coincide with an age of around 2 Gyr.

Chemical abundance variations provide important evidence for (primarily old) stellar population studies (Gratton et al. 2004). Spectroscopic observations of the presence of chemical abundance variations in bright giant stars have provided evidence of Na–O (Carretta et al. 2004; Gratton et al. 2004; Carretta et al. 2009) and Mg–Al anticorrelations (Shetrone 1996). Multimodal stellar distributions in color–magnitude diagrams (CMDs) are observed in some star

clusters. Indeed, many star clusters exhibit two or more parallel sequences in their CMDs (Marino et al. 2008; Piotto et al. 2015), which—for old GCs—have been linked to variations in chemical abundances. Significantly broadened sequences in cluster CMDs could also be indicative of chemical variations, although at the present time conclusive studies are lacking at intermediate ages.

The most common elements that may give rise to multiple parallel sequences in a cluster's CMD and which can be easily traced spectroscopically include He and N (Gratton et al. 2004). Variations in He abundances affect stellar optical luminosities (Gratton et al. 2004), while N abundances determine the ultraviolet (UV) luminosities (Milone et al. 2012a, 2015). Thus, by combining photometry obtained in optical and UV passbands, one could potentially constrain chemical abundance variations in star cluster CMDs.

In this paper, we aim at constraining the maximum chemical abundance spread in an intermediate-age cluster with an age close to the lower boundary of the 2–6 Gyr age range of interest. We considered the suitability of a number of potential target clusters and eventually settled on a careful analysis of NGC 1783. This LMC cluster has an age of approximately 1.8 Gyr (see Section 3.1) and a mass of $1.8 \times 10^5 \ M_\odot$ (Baumgardt et al. 2013). Here, we investigate NGC 1783 using the same methodological approach as Martocchia et al. (2017, 2018). We compare the morphology of the cluster's red-giant branch (RGB) with that of an artificial SSP. As we will see below, the width of the RGB in NGC 1783 is consistent with that expected from an SSP, which implies that the cluster's chemical abundances are essentially single-valued and homogeneous.

We will particularly compare our results with those of (Martocchia et al. 2018). The latter authors have pursued similar research questions based on a large sample of intermediate-age clusters, including NGC 1783. Although their method has a solid mathematical foundation, relying on Gaussian mixture modeling and Akaike information criteria, it is unclear whether their Gaussian peaks have widths that are consistent with the prevailing photometric errors. Our research goes one step beyond their approach by implementing a careful comparison using artificial stars. We point out that our approach is more realistic and based on physical considerations, while fully taking into account the relevant photometric uncertainties. This will allow us to constrain the intrinsic width of the RGB as well as quantify any evidence of broadening, if present.

This paper is organized as follows. In Section 2, we discuss the observations, as well as our data reduction and analysis procedures. In Sections 3 and 4, we present our results and discuss their astrophysical implications. Section 5 summarizes and concludes the paper.

2. DATA REDUCTION

2.1. *Data and Photometry*

We used *Hubble Space Telescope* (*HST*) Advanced Camera for Surveys (ACS)/Wide Field Camera (WFC) and *HST* Ultraviolet Visible channel (UVIS)/Wide Field Camera 3 (WFC3) archival data obtained from the *HST* Legacy Archive. Specifically, we downloaded images obtained through the F336W, F435W, F555W, and F814W filters. For each photometric band, except for the F336W filter, we obtained long- and short-exposure images in order to ameliorate saturation effects. For F336W, we only obtained a long-exposure image; however, this latter image does not suffer from saturation. Images taken with the *HST* ACS/WFC (Proposal ID: GO-10595; Principal Investigator, PI: Goudfrooij) include long- and short-exposure images in the F435W, F555W, and F814W bands. The long exposure times were, respectively, 770 s, 720 s, and 688 s, while the corresponding short exposure times were 90 s, 40 s, and 8 s. Our long-exposure F336W image was taken with the *HST* UVIS/WFC3 (Proposal ID: GO-12257; PI: Girardi), with an exposure time of 3580 s.

We used two independent photometric software packages, i.e., Iraf/DAOPHOT (Stetson 1987) and DOLPHOT (Dolphin 2000), to perform point-spread-function (PSF) photometry on the NGC 1783 images. We compared the outputs of the two packages, concluding that both yield internally consistent photometric results (see also Wu et al. 2016, their Fig. 5). Our subsequent analysis will be based on the DOLPHOT output in the Vegamag photometric system.

We proceeded by following the recommendations in the DOLPHOT manual:[1]

- Mask bad pixels using the `ACSMASK/WFC3MASK` command;

- Split the images according to the chips used for the observations by application of the `SPLITGROUPS` command;

---

[1] http://purcell.as.arizona.edu/dolphot/

- Calculate the sky brightness level using the `CALCSKY` command;

- Proceed to perform PSF photometry using the `DOLPHOT` command. For the ACS/WFC bands (F435W, F555W, and F814W), we performed our photometric approach on all three long-exposure `_flt` images simultaneously, using the drizzled (`_drz`) F435W image as our reference image. We adopted this latter image as our reference since it has the longest exposure time, although we could have taken any of the long-exposure images without suffering from selection biases. We performed PSF photometry separately on the long-exposure F336W `_flt` image.

- Repeat the PSF photometry for the short exposure `_flt` images of the ACS/WFC bands (F435W, F555W, and F814W) with exactly the same approach and the same reference image.

- Combine the catalogs obtained from the different chips.

We only selected objects characterized by sharpness parameters in the output catalog within the range $[-0.3, 0.3]$. The combined F435W, F555W, and F814W long-exposure catalog contained 36,091 stars; the short-exposure catalog included 12,782 stars. From the long-exposure F336W image, we retrieved 32,792 objects.

To cross-identify sources between the catalogs and filters, we applied a critical (maximum) distance of $0.3''$ (~ 6 pixels). The cross matching was done in R.A.–Dec. space, so that any effects associated with image translation and rotation were taken into account properly. Inspection of the histogram of position mismatches between the F336W catalog on the one hand and the combined catalog resulting from the F435W, F555W, and F814W images (which had already been internally aligned to subpixel accuracy) on the other shows that the distribution of positional mismatches peaks around 1.5 pixels: see Fig. 1.
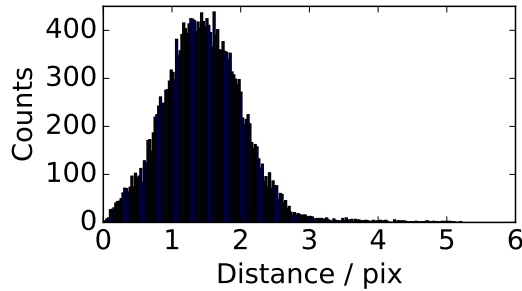

Figure 1. Histogram showing the positional mismatch distribution between the F336W catalog and the combined F435W, F555W, and F814W photometric catalog.

We started by matching the catalogs resulting from the different exposure times. For our short-exposure images, we only adopted those stars characterized by $m_{\mathrm{F435W}} < 19.5$ mag or $m_{\mathrm{F555W}} < 18.8$ mag (a total of 454 objects), since fainter objects are not saturated and, hence, the longer exposure time images are expected to yield more reliable photometry: see Fig. 2 for an example. For unsaturated objects matched in both catalogs, we adopted the long-exposure photometry. Unmatched stars from both the short- and long-exposure images were combined to construct our final catalog, containing 36,206 stars.

We finally cross-identified objects found in different filters using the same procedure. We only retained objects matched in all filters. The matched star catalog with magnitudes in all four photometric bands contains 24,425 stars.

2.2. *Differential Reddening Correction*

Differential reddening corrections were applied to properly deal with the potentially spatially variable foreground reddening. An example to underscore this importance is provided by (Milone et al. 2012b, their Fig. 8). Their results show clear differences in the CMDs—particularly in the widths of the main sequences and RGBs—of several clusters before and after having applied these corrections.

Next, we needed to correct our photometry for the effects of differential reddening. Again, we followed the procedure proposed by (Milone et al. 2012b, their Section 3.1):
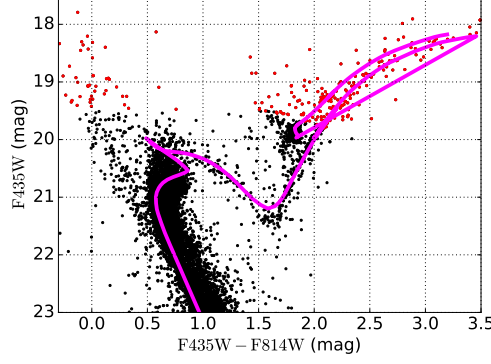
Figure 2. NGC 1783 CMD and best-fitting PARSEC isochrone (Bressan et al. 2012). Black (red) points: stars fainter (brighter) than the saturation level. The physical parameters associated with the best-fitting isochrone are: Age $t = 1.8$ Gyr, distance modulus $(m - M)_0 = 18.46$ mag, and metallicity $Z = 0.007$.

- Rotate the CMD such that the abscissa axis becomes the direction of the differential reddening. The rotation angle can be calculated from the ratio of the extinction effects in the two filters used to construct the CMD;

- Select all stars from a smooth region in the CMD as reference stars. We selected the upper main-sequence region for this purpose (specific magnitude and color limits depend on the passband combination used). We proceeded to fit a central fiducial curve to this smooth region. Note that we only measure relative reddening values, which hence might be negative with respect to the value pertaining to the reference curve. We assume the deviation of each point from the central curve to be fully determined by differential reddening, although—particularly along the main sequence—the presence of binary systems may also contribute to the deviations. However, since we are predominantly interested in the cluster's RGB morphology, this does not affect our results;

- For any star in the catalog, we determine the associated reddening value by averaging the reddening values of its spatially N-nearest reference stars. We adopted $N = 40$ (cf. Milone et al. 2012b).

Since we have access to observations in four filters, thus allowing six passband combinations, we repeated this analysis for each of the six possible pairs of passbands. Hence, we obtained three corrected catalogs for each band; for instance, the F336W catalog was corrected using the combinations $m_{F336W} - m_{F435W}$, $m_{F336W} - m_{F555W}$, and $m_{F336W} - m_{F814W}$. For each star, the average corrected magnitude from all three corrected catalogs was taken as the final, corrected magnitude. As an example, Fig. 3 shows the differential reddening map for the $m_{F555W} - m_{F814W}$ filter combination (see also Milone et al. 2012b, their Fig. 5). This differential reddening map was applied to the uncorrected photometry to obtain the de-reddened CMD.

2.3. Selection of Red Giant Stars

Figure 4 shows how we selected a sample containing lower-RGB stars for subsequent analysis. We only selected stars of similar luminosity or fainter than the cluster's red clump (RC); selection of brighter RGB stars would open up our analysis to contamination by AGB stars. We applied simultaneous parallelogram-based selection in the m_{F336W} versus $m_{F336W} - m_{F814W}$, m_{F435W} versus $m_{F435W} - m_{F555W}$, and m_{F555W} versus $m_{F555W} - m_{F814W}$ CMDs, only retaining RGB stars that were found in all three parallelograms. The relevant magnitude ranges pertaining to our selection of RGB stars were $17.8 < m_{F814W} < 20.0$ mag and $18.85 < m_{F555W} < 20.8$ mag, so that our RGB sample stars cover the range from the bottom of the RGB up to the bright limit of the RC. Although we did not implemented such magnitude cuts in the F336W and F435W bands, the corresponding ranges in these passbands are $20.5 < m_{F336W} < 21.75$ mag and $19.85 < m_{F435W} < 21.55$ mag. These boundaries also determine magnitude ranges from the bottom of the RGB to the RC's upper limit.

The equivalent color ranges used for our RGB selection were $\Delta(m_{F336W} - m_{F814W}) = 0.50$ mag, $\Delta(m_{F435W} - m_{F555W}) = 0.20$ mag, and $\Delta(m_{F555W} - m_{F814W}) = 0.18$ mag, based on RGB color dispersions of 0.076, 0.025, and 0.028 mag, respectively. We selected the precise color boundaries such that the RGB was well separated from the RC;
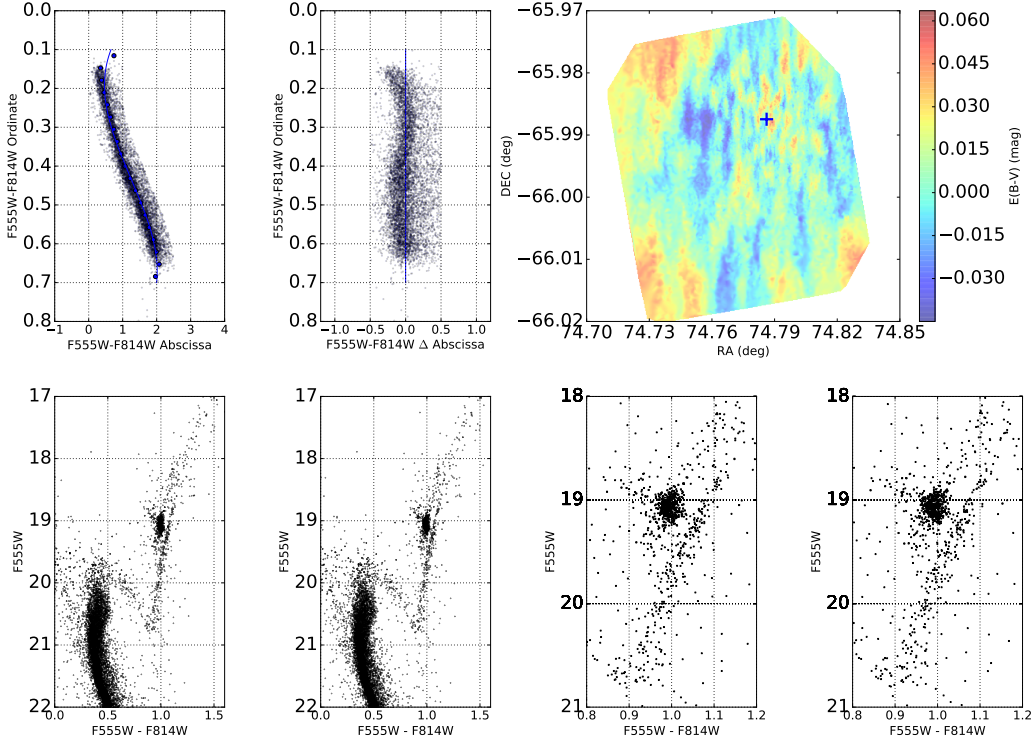
Figure 3. (Top row, left and middle) Fiducial curve fitting and determination of the reddening values for reference stars in abscissa–ordinate space. (Top row, right) Spatial differential reddening map, where the cluster center is marked by a plus sign. The color coding represents the $E(B-V)$ values. (Bottom row, left) CMDs before and after correction. (Bottom row, right) As the two left-hand panels, but focusing on the lower-RGB region.

any rejection of RGB stars owing to photometric errors was minimized by the wide color selection ranges, corresponding to more than five times the observed RGB sample dispersions.

Our lower RGB sample thus selected includes 196 stars; 64 stars were rejected because they were only included in one or two of our selection parallelograms.

2.4. *Field Star Decontamination*

Before quantifying the width of the RGB, we must ensure that our RGB sample is not contaminated by field RGB stars. The cluster's center is located at R.A.$_{J2000}$ = $4^h59^m8.68^s$, Dec.$_{J2000}$ = $-65°59'14.82''$ (Li et al. 2016b). We adopted a cluster radius of $75''$, i.e., three times the cluster's core radius for stars with $m_{F435W} < 23$ mag (Li et al. 2016a).

Our field-star decontamination procedure proceeded on the basis of the following steps (see Fig. 5):

- We determined a field-dominated region outside the cluster's boundary region;

- We then applied the same RGB selection criteria to the cluster and the field CMDs to obtain the equivalent field RGB sample;
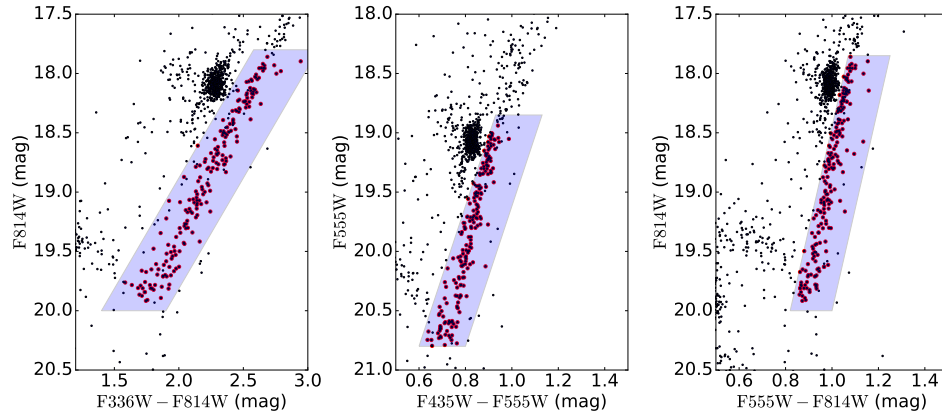
Figure 4. RGB sample selection. Only stars simultaneously found in all three parallelograms were considered for selection.

- We finally statistically subtracted a field component from the distribution of the cluster region RGB sample, taking into account the different areas used for the cluster and field regions. The ratio of the cluster and field regions used was 2.223.

We emphasize that, rather than directly assigning 'field star status to some of our lower-RGB sample and removing them, instead we subtract the C_{index} distribution (which is described in detail in Section 3.2 below) of our field region from the same distribution retrieved from the cluster region.
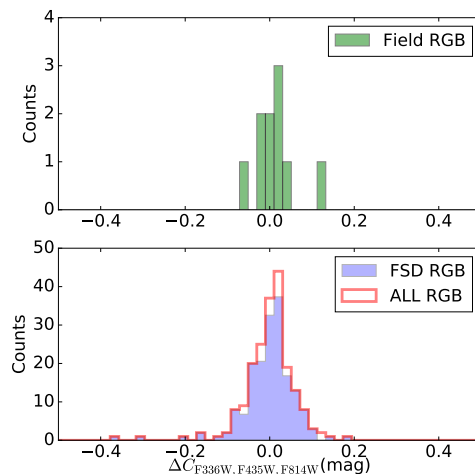

Figure 5. Field-star decontamination and its effect on the C_{index} histogram. (Top) C_{index} histogram of RGB stars in the reference field. (Bottom) Normalized C_{index} histograms of all RGB stars and of the field-star decontaminated (FSD) RGB stars.

3. RESULTS

3.1. *Isochrone Fitting*

We adopted the average extinction, $A_V = 0.06$ mag, and $(m - M)_0 = 18.46$ mag from Li et al. 2016a. We used these values to explore the performance of a set of PARSEC stellar isochrones (Bressan et al. 2012), adjusting their metallicity Z and age t to visually search for the best-matching isochrone. We obtained as best-fitting parameters $t = 1.8 \pm 0.1$ Gyr and $Z = 0.007 \pm 0.001$. The resulting isochrone is overplotted on the CMD in Fig. 2.

Goudfrooij et al. (2011) obtained $t = 1.7 \pm 0.1$ Gyr, while Mackey & Broby Nielsen (2007) determined $t = 1.4 \pm 0.2$ Gyr, $A_V = 0.13$ mag, and $(m - M)_0 = 18.45$ mag. Rubele et al. (2013) obtained $A_V = 0.22$ mag, $(m - M)_0 = 18.57$

mag, and $Z = 0.0065$. Finally, Li et al. 2016a recommended $t = 1.4$ Gyr, $Z = 0.008$, and $A_V = 0.06$ mag. With respect to the latter determination, we believe that our best-fitting metallicity of $Z = 0.007$ is more accurate; we carefully examined the match of our best-fitting isochrone to the cluster's RC. For the best-fitting age of $t = 1.8$ Gyr, the resulting metallicity of $Z = 0.007$ is clearly the best fit.

Second, the age derived by Rubele et al. (2013) was relatively poorly constrained, since it was based on obtaining the optimal fit to the morphology of the extended main-sequence turn-off (Milone et al. 2009). The age difference of 400 Myr implied by our best fit here likely reflects a more accurate age determination, which is constrained by the overall morphology of the cluster CMD, including that of the post-main-sequence evolutionary phases.

3.2. *Artificial Star Tests*

We used artificial star tests to examine whether the full width of the RGB can be explained solely by the photometric uncertainties. Using the best-fitting isochrone and the spatial distribution of the RGB stars, we created an artificial input stellar catalog containing 78,400 stars. We subsequently reran the DOLPHOT photometry using the `-fakestar` option. Of the 78,400 input stars, we recovered 68,800 objects. The 78,400 artificial stars were inserted in 400 sets of 196 objects at a time so as to avoid adding too many artificial stars to the cluster image simultaneously. If we were to overload the science image with artificial stars, unrealistically high blending ratios and background levels would result.

We examined the observed and artificial RGB sequences by plotting their magnitudes versus their color index; the latter is the color defined by the objects' magnitudes in three bands, i.e., $C_{\mathrm{F336W,F435W,F814W}} = (m_{\mathrm{F336W}} - m_{\mathrm{F435W}}) - (m_{\mathrm{F435W}} - m_{\mathrm{F814W}})$. Second-generation stars are expected to have higher N and He abundances, and lower C abundances, than first-generation stars. Their $(m_{\mathrm{F435W}} - m_{\mathrm{F814W}})$ colors will hence become bluer because of the increased temperatures caused by more abundant He, while the $(m_{\mathrm{F336W}} - m_{\mathrm{F435W}})$ colors will become redder owing to a nitrogen absorption band found within the F336W filter bandpass, which is enhanced by the higher N abundance. Therefore, these differences between both generations of stars add up in the $C_{\mathrm{F336W,F435W,F814W}}$ combination, which is thus a good choice to probe chemical abundance variations associated with MSPs. Such double-peak features in the C_{index} distributions of the RGB have been discovered in, e.g., NGC 121 (Niederhofer et al. 2017a) and NGC 1978 (Martocchia et al. 2018)—based on the use of similar instruments and exposure times as done in this paper—which has been interpreted as clear evidence of dual chemical abundance components. This indicates that application of the C_{index} is indeed a suitable approach to detect chemical abundance variations and that the absence of a C_{index} dispersion implies a lack of evidence of any abundance variations in one's cluster of interest.

To generate the input artificial stellar catalog, we proceeded as follows:

- We assigned random coordinates to the artificial stars based on a random selection of 196 lower-RGB stars in our observed sample;

- To avoid spatial overlaps with any of the observed lower-RGB stars, we added random perturbations to these coordinates. We adopted perturbations equivalent to half the distance of any of the selected lower-RGB stars to their (spatially) closest lower-RGB star in our sample.

- We assigned magnitudes to the artificial stars based on the closest-matching segment of the best-fitting PARSEC isochrone. We interpolated this segment uniformly (i.e., we adopted a curve in the four-dimensional space defined by the F336W, F435W, F555W, and F814W magnitudes), for the entire artificial-star catalog.

- Finally, we matched the coordinates randomly with the resulting magnitudes to complete our input artificial RGB star catalog.

We next used DOLPHOT to obtain PSF photometry for the artificial stars we just inserted into the science images and generated the corresponding output photometric catalog. This procedure is fully equivalent to that adopted for the real stars in Section 2.1.

The results of our artificial-star analysis can also be used to estimate the completeness levels of our observations. We recovered 68,880 of the 78,400 input stars, so the completeness level of our RGB sample is approximately 88%. Figure 2 shows that the photometric detection limit is significantly fainter than $m_{\mathrm{F435W}} = 23$ mag. Our RGB sample is significantly too bright to be affected by the detection limit, but at the RGB level incompleteness may be caused by crowding effects (blending) instead.

3.3. Broadening of the Red Giant Branch

We will now examine if the RGB of NGC 1783 is consistent with a single metallicity using a similar approach as Niederhofer et al. (2017b). We start by comparing the corresponding artificial stellar population and the observed RGB population in the m_{F814W} versus $C_{\mathrm{F336W,F435W,F814W}}$ diagram: see Fig. 6, where we have also added a small translation in color to the artificial stars' RGB ridgeline to match it to the ridgeline of the observed RGB stars. The majority of the artificial stars is concentrated well within the observed RGB width, while only a small fraction is characterized by a wide color spread caused by blending. The tight, observed RGB sequence is visually consistent with the single-component distribution of the artificial stars.
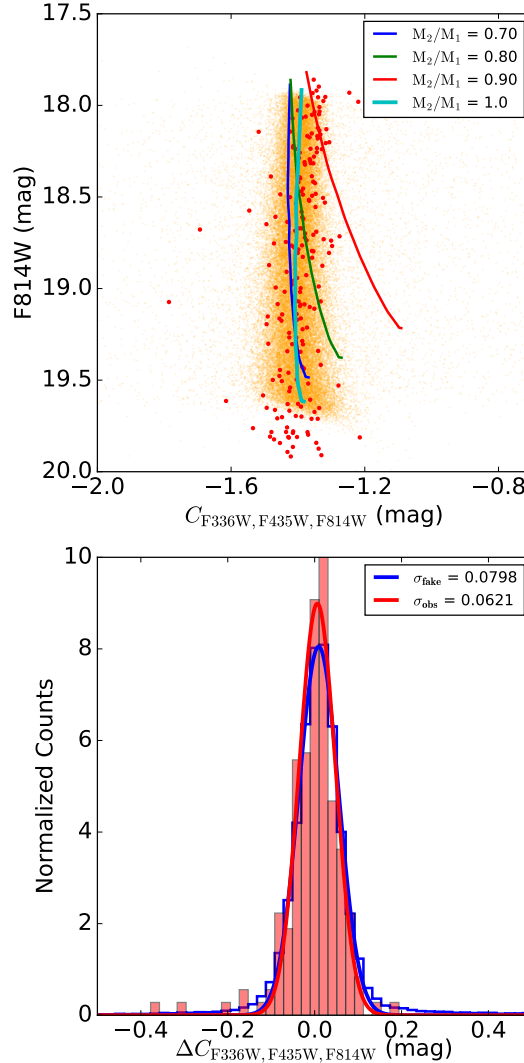

Figure 6. (Top) Comparison of the artificial stellar sample (orange) with the observed RGB sample in the m_{F814W} versus $C_{\mathrm{F336W,F435W,F814W}}$ diagram. A set of binary sequences, adopting different secondary-to-primary mass ratios (see the legend) are also shown. The two stars at the far left cannot be binary systems, but they may be field stars. (Bottom) Normalized histograms showing the deviations from the ridgelines of both the observed RGBs (196 stars) and the artificial stars (68,880 stars representing an SSP).

We next overplotted the observed RGB broadening histogram (i.e., the deviation from the ridgeline, $\Delta C_{\mathrm{F336W,F435W,F814W}}$) and that defined by the artificial stars, both normalized. We fitted Gaussian curves to both distributions. We used a bootstrapping method, repeating the procedure 1000 times, to measure the Gaussian widths and their associated uncertainties. The best-fitting Gaussian standard deviations corresponding the observed and artificial RGB C_{index}

distributions are $\sigma_{\mathrm{obs}} = 0.062 \pm 0.009$ mag and $\sigma_{\mathrm{fake}} = 0.080 \pm 0.001$ mag, respectively. Both distributions have similar widths (see the bottom panel of Fig. 6). Next, we investigated the fraction of observed RGB stars that could be reproduced by the artificial stellar distribution in Fig. 7. We found that the $[-1\sigma_{\mathrm{fake}}, \ 1\sigma_{\mathrm{fake}}]$ interval contains 84% of the observed stars, while the $[-3\sigma_{\mathrm{fake}}, \ 3\sigma_{\mathrm{fake}}]$ interval includes 99% of the observed stars.
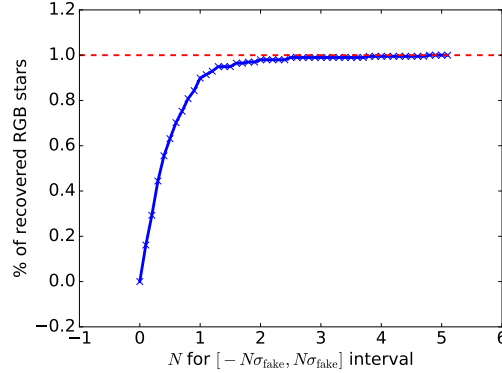
Figure 7. Fraction of the observed RGB stars recovered as a function of the interval covered with respect to the $\Delta C_{\mathrm{F336W,F435W,F814W}}$ distribution; σ_{fake} is the dispersion of the $C_{\mathrm{F336W,F435W,F814W}}$ Gaussian distribution of the artificial stars.

Next, we adjusted our RGB selection criteria to test whether our initial selection had excluded real RGB stars and, if so, how that might affect our results, particularly as regards the width of the RGB. We shifted the upper edges of our RGB selection box slightly to bluer colors in $(m_{\mathrm{F336W}} - m_{\mathrm{F814W}})$ and $(m_{\mathrm{F555W}} - m_{\mathrm{F814W}})$ but not in $(m_{\mathrm{F435W}} - m_{\mathrm{F555W}})$. This adjusted choice leads to the inclusion of a number of RGB stars that are located close to the selection boundary, while retaining the color selection in $(m_{\mathrm{F435W}} - m_{\mathrm{F555W}})$ will still lead to rejection of RC stars. The RGB sample resulting from this updated selection run includes 207 stars. We repeated all of our subsequent analysis and found a new C_{index} value of 0.063 mag, which is almost the same as our initial result, $C_{\mathrm{index}} = 0.062$ mag. We therefore conclude that the potential loss of a small number of genuine RGB stars by our initial selection method does not significantly influence our measurement of the cluster's RGB broadening, nor our final results.

4. DISCUSSION

Our results show that the artificial stellar population is characterized by a similar dispersion in $C_{\mathrm{F336W,F435W,F814W}}$ as the observed RGB sequence of NGC 1783. This demonstrates that the photometric uncertainties fully account for the RGB's broadening in NGC 1783.

The color index used, $C_{\mathrm{F336W,F435W,F814W}}$, is sensitive to the stellar N and He abundances, which are two of the most representative elements that exhibit large abundance variations in star clusters (Gratton et al. 2004). The consistency of the observed RGB's width with that defined by our artificial SSP therefore indicates that our RGB sample is best represented by single-valued N and He abundances.

There are a small number of outliers in the observed RGB distribution, in particular two stars at the far left (see the top panel of Fig. 6). These objects are unlikely statistical fluctuations, given that they deviate by $> 5\sigma$ from the Gaussian peak. Alternatively, they might be field stars that have not been properly removed by our field-star decontamination algorithm. If they were cluster members, they would need to have unrealistically extreme metallicities. Note that these two data points appear both in the scatter diagram in the top panel of Fig. 6 and in the observed histogram in the figure's bottom panel. We suspect that these two stars might result from stochasticity in the field's RGB sample (see Fig. 5) rather than from random effects associated with our field-star decontamination.

We explored whether these objects might be binary systems instead. If we assume that the primary components (M_1) of such binary systems are genuine RGB stars, the secondary components (M_2) must have lower masses. We tested the appearance of binary systems with different mass ratios, M_2/M_1. For very low-mass companions, the change in color is almost negligible, while for equal-mass binaries no color difference is expected compared with the single-star case. The top panel of Fig. 6 includes binary sequences for $M_2/M_1 = 0.7, 0.8$, and 0.9. It is clear that the outliers at the far left cannot be binary systems.

An intermediate-age cluster with an age of 1.8 Gyr and a mass of 1.8×10^5 $M_\odot$, NGC 1783 is comparably massive as other star clusters that show clear evidence of MSPs (e.g., Martocchia et al. 2018). If we assume that mass is an important driver of MSP formation, then NGC 1783 should also have shown clear evidence of chemical abundance variations. However, we have found no such evidence in NGC 1783, which challenges the idea that mass may be a primary driver of MSP formation. The similarity of the observed RGB width in NGC 1783 with that expected for an SSP suggests the absence of chemical abundance variations. When combined with similar results for NGC 419, NGC 1806, and NGC 1846 (Martocchia et al. 2017, 2018), this is indeed inconsistent with mass being a primary driver.

To quantitatively account for the amount of mass loss during the evolution of a star cluster like NGC 1783, we calculated the fractional mass loss expected for NGC 1783 from its present age of 1.8 Gyr to a more advanced age of 6 Gyr following (Lamers et al. 2005, their equations 1, 2, 3, and 6). Unfortunately, the parameter t_4^{dis}, i.e., the dissolution timescale of a cluster with a mass of 10^4 $M_\odot$, is poorly constrained for the LMC, $t_4^{\mathrm{dis}} > 1$ Gyr (Parmentier & de Grijs 2008). Therefore, we investigated a wide range of choices for t_4^{dis}, from 1 to 10 Gyr. We followed the evolution of the cluster's initial mass to ages of 1.8 Gyr and 6 Gyr; we then calculated the ratio of both values: see Fig. 8. The smallest remaining mass fraction from 1.8 Gyr to 6.0 Gyr is 60%, corresponding to a lowest remaining mass of 1.08×10^5 $M_\odot$ by the time the cluster will have evolved to an age of 6 Gyr. Note that (Bekki 2017) suggest that NGC 1783 may be capable of retaining a significant fraction of its gas component (e.g., gas generated by AGB ejecta), thus rendering our estimate a lower limit.
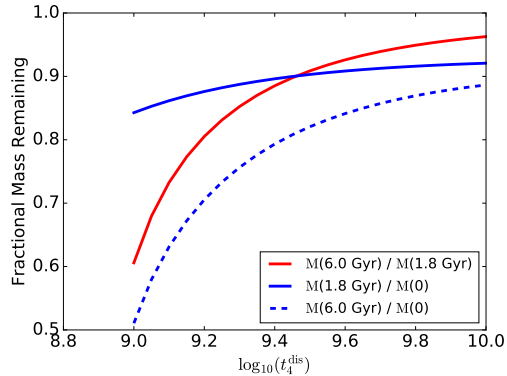

Figure 8. Fractional mass remaining for NGC 1783 from its formation to ages of 1.8 Gyr and 6.0 Gyr (blue curves), and from 1.8 Gyr to 6.0 Gyr (red).

If we assume mass to be an important driver for the formation of MSPs, then given our conclusion that the remaining mass of NGC 1783 at 6 Gyr is likely at least 1.08×10^5 $M_\odot$, we should expect to find no evidence of chemical abundance variations in other, similarly massive clusters with ages of around 6 Gyr. However, MSPs seem to be ubiquitous for GCs older than 6 Gyr (Milone et al. 2017, their Fig. 23)). For instance, NGC 339—an SMC cluster with an age of 6.3 Gyr and a mass of 0.83×10^5 $M_\odot$—has been reported to host MSPs (Niederhofer et al. 2017a, their Fig. 4). Therefore, a comparison of NGC 1783 with NGC 339 (and clusters with similar properties) suggests that the idea of mass as a primary driver is not borne out by the data. Although our result is consistent with age being a primary factor (Martocchia et al. 2018), NGC 1783 only represents a single data point so that we caution against overinterpretation of these results.

Finally, the physical reality at the old age of genuine GCs may well be rather different from that at the younger ages of the cluster we have just investigated. (Milone et al. 2017) suggested that mass may be an important driver of MSPs in a sample of old Milky Way GCs. They found clear correlations of both the fractional number and the RGB pseudo-color width of the second-generation stars with their host clusters' masses. Note, however, that chemical abundance variations are only well established for old GCs; at the younger ages discussed in this paper, we only have circumstantial evidence of possible MSPs based on the broadening of distinct CMD features, not of clearly distinct sequences.

5. SUMMARY AND CONCLUSIONS

Using *HST* photometry, we have compared the C_{index} dispersion of our observed RGB sample with an artificial SSP, and found their widths to be fully consistent with one another. We adopted a color index that is sensitive to N and He abundance variations, so the observed consistency indicates the absence of N and He abundance variations, two elements whose abundances tend to vary most in star clusters in general.

Our results thus indicate that an SSP model is sufficient to explain the RGB broadening in NGC 1783. We explored the possible nature of two outliers in the RGB distribution and concluded that they are most likely field stars.

An intermediate-age cluster with an age of 1.8 Gyr and a mass of $1.8 \times 10^5 \ M_{\odot}$, NGC 1783 is comparably massive as other star clusters that show clear evidence of MSPs. After incorporating mass-loss recipes from an age of 1.8 Gyr to a more advanced age of 6 Gyr, NGC 1783 is expected to remain as massive as some other clusters that host clear MSPs.

If we assume that mass is an important driver of MSP formation, then NGC 1783 should have shown clear evidence of chemical abundance variations. However, we found no such evidence in NGC 1783. This result is in agreement with the properties of other massive clusters of similar age.

ACKNOWLEDGEMENTS

REFERENCES

Anderson, J., Piotto, G., King, I. R., Bedin, L. R., & Guhathakurta, P. 2009, ApJL, 697, L58

Balbinot, E., Santiago, B. X., Kerber, L. O., Barbuy, B., & Dias, B. M. S. 2010, MNRAS, 404, 1625

Bastian, N., Cabrera-Ziri, I., Davies, B., & Larsen, S. S. 2013, MNRAS, 436, 2852

Bastian, N., Cabrera-Ziri, I., & Salaris, M. 2015, MNRAS, 449, 3333

Bastian, N., & Goodwin, S. P. 2006, MNRAS, 369, L9

Bastian, N., & Strader, J. 2014, MNRAS, 443, 3594

Bate, M. R., Bonnell, I. A., & Bromm, V. 2003, MNRAS, 339, 577

Baumgardt, H., & Kroupa, P. 2007, MNRAS, 380, 1589

Baumgardt, H., Parmentier, G., Anders, P., & Grebel, E. K. 2013, MNRAS, 430, 676

Bedin, L. R., Piotto, G., Zoccali, M., et al. 2000, A&A, 363, 159

Bekki, K. 2017, MNRAS, 467, 1857

Bekki, K., & Mackey, A. D. 2009, MNRAS, 394, 124

Bressan, A., Marigo, P., Girardi, L., et al. 2012, MNRAS, 427, 127

Cabrera-Ziri, I., Bastian, N., Davies, B., et al. 2014, MNRAS, 441, 2754

Cabrera-Ziri, I., Lardo, C., Davies, B., et al. 2016, MNRAS, 460, 1869

Cabrera-Ziri, I., Bastian, N., Longmore, S. N., et al. 2015, MNRAS, 448, 2224

Carretta, E., Bragaglia, A., & Cacciari, C. 2004, ApJL, 610, L25

Carretta, E., Bragaglia, A., Gratton, R. G., et al. 2009, A&A, 505, 117

Charbonnel, C., Krause, M., Decressin, T., Prantzos, N., & Meynet, G. 2013, Mem. Soc. Astron. Italiana, 84, 158

Davidge, T. J. 2012, ApJ, 761, 155

Denissenkov, P. A., & Hartwick, F. D. A. 2014, MNRAS, 437, L21

D'Ercole, A., Vesperini, E., D'Antona, F., McMillan, S. L. W., & Recchi, S. 2008, MNRAS, 391, 825

Dolphin, A. E. 2000, PASP, 112, 1383

Farias, J. P., Smith, R., Fellhauer, M., et al. 2015, MNRAS, 450, 2451

Geisler, D., Bica, E., Dottori, H., et al. 1997, AJ, 114, 1920

Goudfrooij, P., Puzia, T. H., Kozhurina-Platais, V., & Chandar, R. 2011, ApJ, 737, 3

Gratton, R., Sneden, C., & Carretta, E. 2004, ARA&A, 42, 385

Harris, W. E. 1996, AJ, 112, 1487

Hong, J., de Grijs, R., Askar, A., et al. 2017, MNRAS, 472, 67

Jiang, D., Han, Z., & Li, L. 2014, ApJ, 789, 88

Lamers, H. J. G. L. M., Gieles, M., Bastian, N., et al. 2005, A&A, 441, 117

Li, C., de Grijs, R., Deng, L., et al. 2016a, Nature, 529, 502

Li, C.-Y., de Grijs, R., & Deng, L.-C. 2016b, Research in Astronomy and Astrophysics, 16, 179

Lima, E. F., Bica, E., Bonatto, C., & Saito, R. K. 2014, A&A, 568, A16

Mackey, A. D., & Broby Nielsen, P. 2007, MNRAS, 379, 151

Marino, A. F., Villanova, S., Piotto, G., et al. 2008, A&A, 490, 625

Martocchia, S., Bastian, N., Usher, C., et al. 2017, MNRAS, 468, 3150

Martocchia, S., Cabrera-Ziri, I., Lardo, C., et al. 2018, MNRAS, 473, 2688

McLaughlin, D. E., & van der Marel, R. P. 2005, ApJS, 161, 304

Milone, A. P., Bedin, L. R., Piotto, G., & Anderson, J. 2009, A&A, 497, 755

Milone, A. P., Piotto, G., Bedin, L. R., et al. 2012a, ApJ, 744, 58

—. 2012b, A&A, 540, A16

Milone, A. P., Marino, A. F., Piotto, G., et al. 2015, MNRAS, 447, 927

Milone, A. P., Piotto, G., Renzini, A., et al. 2017, MNRAS, 464, 3636

Mucciarelli, A., Carretta, E., Origlia, L., & Ferraro, F. R. 2008, AJ, 136, 375

Niederhofer, F., Bastian, N., Kozhurina-Platais, V., et al. 2017a, MNRAS, 465, 4159

—. 2017b, MNRAS, 464, 94

Parmentier, G., & de Grijs, R. 2008, MNRAS, 383, 1103

Pflamm-Altenburg, J., & Kroupa, P. 2009, MNRAS, 397, 488

Piotto, G., Milone, A. P., Marino, A. F., et al. 2013, ApJ, 775, 15

Piotto, G., Bedin, L. R., Anderson, J., et al. 2007, ApJL, 661, L53

Piotto, G., Milone, A. P., Bedin, L. R., et al. 2015, AJ, 149, 91

Rubele, S., Girardi, L., Kozhurina-Platais, V., et al. 2013, MNRAS, 430, 2774

Shetrone, M. D. 1996, AJ, 112, 1517

Stetson, P. B. 1987, PASP, 99, 191

Vesperini, E., McMillan, S. L. W., D'Antona, F., & D'Ercole, A. 2013, MNRAS, 429, 1913

Worthey, G. 1994, ApJS, 95, 107

Wu, X., Li, C., de Grijs, R., & Deng, L. 2016, ApJL, 826, L14